

Solar Energy

Enhancing the filling of perovskite material in the scaffold layer to improve the conversion efficiency of printable perovskite solar cells

--Manuscript Draft--

Manuscript Number:	SEJ-D-25-00611
Article Type:	Research paper
Section/Category:	Photovoltaic Cells and Cell Physics
Keywords:	Printed mesoscopic perovskite solar cells; Filling dynamics; Infiltration; Crystallization
Abstract:	<p>The complete filling of perovskite materials into mesoporous TiO₂/ZrO₂ scaffold film remains a great challenge for achieving a high conversion efficiency in printed mesoscopic perovskite solar cells. However, there is a lack of a precise understanding of the filling dynamics to guide the optimization process. In this study, a process comprising the beginning infiltration step and the subsequent crystallization step have been proposed to optimize filling behavior. By introducing macropores in the first step using the polystyrene microsphere templating method to facilitate the infiltration of the perovskite precursor solution, combined with the bottom-up controlled crystallization assisted by a low-pressure gas pumping method in the second step, the perovskite material is more completely filled into the TiO₂/ZrO₂ scaffold layer. The photovoltaic performance of the perovskite solar cell shows that the conversion efficiency is improved by 375% compared to the weakly filled solar cells. This work contributes to enhance the filling of perovskite material and improve the conversion efficiency of printable perovskite solar cells.</p>

Enhancing the filling of perovskite material in the scaffold layer to improve the conversion efficiency of printable perovskite solar cells

Weiwu Dang¹, Li Liu², Jianhua Chen², Xian Gu², Xuhao Wang², Xiaolan Li²,
Yan Li^{2, *}

¹College of Intelligent Manufacturing, Shaanxi Institute of Technology, Xi'an, Shaanxi 710300, China

²College of New Energy, Xi'an Shiyou University, Xi'an, Shaanxi 710065, China

* Correspondence to: Doc. Yan Li, College of New Energy, Xi'an Shiyou University, Xi'an, Shaanxi 710065, China

E-mail address: li1988yan@163.com

Abstract: The complete filling of perovskite materials into mesoporous TiO₂/ZrO₂ scaffold film remains a great challenge for achieving a high conversion efficiency in printed mesoscopic perovskite solar cells. However, there is a lack of a precise understanding of the filling dynamics to guide the optimization process. In this study, a process comprising the beginning infiltration step and the subsequent crystallization step have been proposed to optimize filling behavior. By introducing macropores in the first step using the polystyrene microsphere templating method to facilitate the infiltration of the perovskite precursor solution, combined with the bottom-up controlled crystallization assisted by a low-pressure gas pumping method in the second step, the perovskite material is more completely filled into the TiO₂/ZrO₂ scaffold layer. The photovoltaic performance of the perovskite solar cell shows that the conversion efficiency is improved by 375% compared to the weakly filled solar cells. This work contributes to enhance the filling of perovskite

material and improve the conversion efficiency of printable perovskite solar cells.

Keywords: Printed mesoscopic perovskite solar cells; Filling dynamics; Infiltration; Crystallization

1. Introduction

The commercial-scale production of perovskite solar cells (PSCs) has attracted widespread attention^{1,2}. The printed mesoscopic PSCs with an all-mesoporous structure can be directly fabricated in the air using a screen printing technique³⁻⁵, which is a promising candidate for the commercialization of solar cells. Years ago, when Han's group⁶ introduced $(5\text{-AVA})_x\text{CH}_3\text{NH}_3(1-x)\text{PbI}_3$ as the light-absorbing material, achieving a conversion efficiency of 10.4% in solar cells with an active cell area of 49 cm². Furthermore, it has been reported that the printed mesoscopic PSCs can keep their initial efficiency unchanged during 1000 hours of light exposure, and these solar cells exhibit long-term stability, lasting over one year in the dark due to the hydrophobic nature of carbon electrodes⁶. Studies also indicate that these solar cells retain more than 97% of their initial efficiency after 2,136 hours under outdoor conditions⁷, and the printable PSCs have passed the widely recognized international standard IEC61215:2016⁸. Nowadays, Wonder Solar Ltd. demonstrates a 110 m² fully printable mesoscopic PSCs outdoor power generation system⁹. Researchers believe that printable mesoscopic PSCs are strong contenders for the commercialization of perovskite solar cells.^{10,11}

1 In the printed mesoscopic PSCs, removing the hole transport material and
2
3 replacing the silver/gold electrode with a carbon electrode can reduce the cost of the
4
5 solar cells and simplify the fabrication process¹²⁻¹⁵. However, preparation of the carbon
6
7 electrode requires a high-temperature treatment at 400°C, which is higher than the
8
9 decomposition temperature of the perovskite materials. Therefore, in the solar cell
10
11 assembly process, the carbon electrode is first deposited onto the TiO₂/ZrO₂ scaffold
12
13 layer, after which the perovskite, serving as the light-absorbing material, is infiltrated
14
15 into the scaffold film using a solution-based method¹⁶⁻¹⁸. However, the extent to which
16
17 perovskite fills the scaffold film is crucial for the performance and stability of the fully
18
19 printable PSCs¹⁹⁻²¹. A completely filling and good connectivity of the perovskite
20
21 material in the scaffold film enhances its ability to capture photonic energy, dissociating
22
23 excitons via the MAPbI₃/TiO₂ heterojunction, and transport holes to carbon electrode,
24
25 whereas insufficient filling of the perovskite material in the TiO₂/ZrO₂ scaffold film
26
27 leads to poor light absorption, discontinuous carrier transport channels, and severe
28
29 internal recombination^{22,23}.
30
31
32
33
34
35
36
37
38
39
40
41

42 The filling amount of perovskite material is influenced by multiple factors, such
43
44 as the uncontrolled crystallization of the precursor solution²⁴, the pore structure of the
45
46 mesoporous scaffold layer^{25,26}, the filling process²⁷ and the interfacial contact between
47
48 the perovskite and the mesoporous scaffold layer^{28,29}. Many researchers have attempted
49
50 to manipulate the perovskite precursor, such as Chen et al.³⁰ systematically investigated
51
52 the impact of various solvents on the filling behavior, and achieved a conversion
53
54 efficiency of 13.89% by optimizing the ratio of dimethylformamide (DMF) and
55
56
57
58
59
60
61
62
63
64
65

1 dimethyl sulfoxide (DMSO). This optimization improved the wettability and stabilized
2
3 the mesophase of the perovskite precursor, thereby regulating the crystallization rate of
4
5 perovskite crystals. Rong et al.³¹ utilized pure DMSO as a solvent due to its strong
6
7 coordination ability and the formation of a stable intermediate phase (PbI₂-DMSO-
8
9 CH₃NH₃I) to dissolve perovskite. This approach effectively inhibited the rapid binding
10
11 of PbI₂ and CH₃NH₃I while accelerating the infiltration of the perovskite precursor into
12
13 the scaffold layer. In addition to the manipulation of the solvent, previous results have
14
15 demonstrated that both pore blockage caused by preferential perovskite crystallization
16
17 and solvent retention can lead to incomplete filling of the scaffold film³². Bogachuk et
18
19 al.³³ introduced a sacrificial Polystyrene nanoparticles film into the scaffold film to
20
21 create nano-cavities enabling the growth of larger perovskite crystals inside the oxide
22
23 scaffold. However, achieving complete filling of perovskite materials into the
24
25 TiO₂/ZrO₂ scaffold film is still a great challenge. To reach a fully filled state, a precise
26
27 understanding of the physical dynamics involved is still required. Moreover, the
28
29 correlation between solution infiltration and precursor crystallization has yet to be fully
30
31 established, and the corresponding regulatory mechanisms governing these processes
32
33 remain unexplored.
34
35
36
37
38
39
40
41
42
43
44
45
46

47 In the study, based on the observed filling behavior of CH₃NH₃PbI₃ (MAPbI₃) into
48
49 the TiO₂/ZrO₂ scaffold film, the physical filling dynamics were analyzed. The
50
51 correlation between infiltration and crystallization in enhancing the perovskite
52
53 materials filling was established. To optimize this process, sub-macropores were
54
55 introduced into the scaffold layer using the Polystyrene microsphere templating method,
56
57
58
59
60
61
62
63
64
65

and followed by bottom-up controlled crystallization facilitated by a low-pressure gas pumping method. At last, the photovoltaic performance of the PSCs was evaluated.

2. Experimental

2.1 Materials

Zirconium oxide (ZrO_2) powder and titanium dioxide (TiO_2) powder were purchased from Degussa AG (Germany). N-butanol ($\text{C}_4\text{H}_{10}\text{O}$), terpineol ($\text{C}_{10}\text{H}_{18}\text{O}$), ethyl cellulose ($(\text{C}_{12}\text{H}_{22}\text{O}_5)_n$) and acetone ($\text{C}_3\text{H}_6\text{O}$) were purchased from Shanghai Reagent Chemical Co., Ltd (China). Lead iodide (PbI_2), methylamine iodide ($\text{CH}_3\text{NH}_3\text{I}$, MAI), N,N-dimethylformamide ($\text{C}_3\text{H}_7\text{NO}$, DMF), TiO_2 compact layer precursor solution and hole transport material (HTM) were purchased from Xi'an Yuri Solar Co., Ltd (China). The transparent fluorine-doped tin oxide (FTO, TEC-15, $25 \times 25 \text{ mm}^2$, LOF) conductive glass was used as substrates. The polystyrene (PS) microspheres of $\sim 300 \text{ nm}$ were purchased from Rigor Science Co., Ltd (China). The HTM is composed of 80 mg of spiro-OMeTAD, 28.5 ml of 4-tert-butylpyridine, and 17.5 ml of lithium bis(trifluoromethanesulfonyl)imide (Li-TFSI) solution (520 mg of Li-TFSI in 1 ml of acetonitrile), all of which were dissolved in 1 ml of chlorobenzene.

2.2 Preparation of the TiO_2 and ZrO_2 slurry

For the ZrO_2 slurry, firstly, 0.45 g of ethyl cellulose and 0.6 ml terpineol was dissolved into 5 ml of n-butanol to prepare an ethyl cellulose solution, and 2.5 g of ZrO_2 was dispersed in n-butanol to form a 35 wt% suspension. Secondly, the ethyl cellulose solution and ZrO_2 suspension were mixed by magnetic stirring for 12 h, followed by grinding for 20 min to obtain a ZrO_2 slurry. In order to increase the porosity of the ZrO_2

1 film by 25%, 0.16 g of PS microspheres was added in the second step.

2
3 For the TiO₂ slurry, except that 1.5 g of TiO₂ was dispersed in n-butanol to form a
4
5
6 20 wt% suspension in the first step, the other steps follow the same preparation process
7
8
9 as ZrO₂ slurry. In order to increase the porosity of the TiO₂ film by 25%, 0.07 g of PS
10
11
12 microspheres was added in the second step.

13 14 **2.3 Filling the perovskite into the scaffold film and fabrication of the PSCs**

15
16
17 The FTO was cleaned successively in deionized water and alcohol, and dried with
18
19
20 N₂ flow. A compact TiO₂ layer was deposited on the etched FTO substrate via spin
21
22
23 coating and then annealed at 120°C for 15 min. Subsequently, the TiO₂ films and ZrO₂
24
25
26 films were deposited using screen-printing technique, and then annealed in a tube
27
28
29 furnace at 400°C for 30 min to produce the TiO₂/ZrO₂ scaffold films. Then, the carbon
30
31
32 film was also deposited using screen-printing technique, and annealed in a tube furnace
33
34
35 at 450°C for 30 min.

36
37 The MAPbI₃ precursor solution was prepared by dissolving PbI₂ and CH₃NH₃I in
38
39
40 DMF at a concentration of 460 mg·mL⁻¹, which was infiltrated from the carbon side,
41
42
43 and subsequently spin-coated at 3000 rpm for 10 s. To keep the bottom-up
44
45
46 crystallization of the perovskite material, the sample was transferred to the low-pressure
47
48
49 chamber of the low-pressure gas pumping equipment³⁴⁻³⁶ and dried at 1000 Pa for 10
50
51
52 min. Finally, the PSCs were annealed at 120°C for 10 min. All the above processes were
53
54
55 carried out at a low temperature of 2-3°C.

56 57 **2.4 Characterization**

58
59 The phase structures of the TiO₂ and ZrO₂ films were measured by an X-ray
60
61
62
63
64
65

1 diffractometer using Cu K α radiation (XRD, Bruker–D8 ADVANCE, Germany). The
2
3 morphology of the scaffold film was characterized using a scanning electron
4
5 microscope (SEM, ZEISS Sigma 300, Germany). To quantitatively analyze the
6
7 elemental distribution in perovskite, energy-dispersive X-ray spectroscopy (EDS,
8
9 Oxford Xplore 30, United Kingdom) was employed. The current density-voltage (J - V)
10
11 characteristics of the solar cells were measured using a solar simulator (100 mW·cm⁻²,
12
13 Oriel 94023A, Newport) equipped with a Keithley 2400 digital source meter. The exact
14
15 light intensity was calibrated using a single-crystal silicon reference photovoltaic cell
16
17 (91150V, Oriel Instruments).
18
19
20
21
22
23
24

25 **3. Results and discussion**

26 **3.1 Perovskite material tends to accumulate in the upper region of the scaffold film**

27
28 The TiO₂/ZrO₂ scaffold film was prepared using the screen-printing technique,
29
30 and the XRD patterns of both films deposited on the FTO substrate are shown
31
32 separately in Figure S1. The cross-sectional views of typical scaffold films at high and
33
34 low magnifications are shown in Figure S2. As can be seen, it exhibits a bilayer
35
36 morphology, where the bottom TiO₂ layer is fully covered by the upper ZrO₂ layer. In
37
38 common planar-structure PSCs, a perovskite film thickness of approximately 400 nm
39
40 is required for sufficient light absorption³⁷. When a comparable amount of perovskite
41
42 material is incorporated into the scaffold film, its thickness must be significantly
43
44 increased to the micrometer level. The increased thickness of the scaffold film ensures
45
46 efficient electron extraction from the perovskite absorber, ultimately reducing hole
47
48 accumulation and mitigating severe carrier recombination.
49
50
51
52
53
54
55
56
57
58
59
60
61
62
63
64
65

1 Considering that the carbon film has a thickness of tens of micrometers and a pore
2
3 size in the micrometer range, it barely affects the complete filling of the perovskite
4
5 material³⁸. Therefore, in the following analysis, the filling behavior is investigated
6
7 exclusively based on the TiO₂/ZrO₂ scaffold film. After MAPbI₃ is incorporated into
8
9 the TiO₂/ZrO₂ scaffold film, the filling results are characterized by EDS. Seven targets
10
11 were selected, as shown in Fig. 1(a), with detailed measurement results presented in
12
13 Table S1. The comparative weight percentage distributions of Ti, Zr, O, Pb, I, Sn, and
14
15 F from top to bottom in the scaffold film are shown in Fig. 1(b). It is observed that the
16
17 distribution profiles of Ti and Zr are in good agreement with the morphology results in
18
19 Fig. 1(a), confirming the validity of the characterization. The distributions of Pb and I
20
21 were analyzed and found to be mainly concentrated on the upper surface, indicating
22
23 that MAPbI₃ does not penetrate into the inner part of the scaffold film. A comparative
24
25 study on a thinner scaffold film was also conducted, as shown in Figure S3. The
26
27 thickness of the TiO₂/ZrO₂ scaffold film was reduced from ~8 μm to ~4 μm, which is
28
29 comparable to reported results, yet the perovskite material still cannot penetrate deep
30
31 into its interior. This suggests that the thickness of the TiO₂/ZrO₂ scaffold film is not
32
33 the primary factor determining the filling amount.
34
35
36
37
38
39
40
41
42
43
44
45
46
47
48
49
50
51
52
53
54
55
56
57
58
59
60
61
62
63
64
65

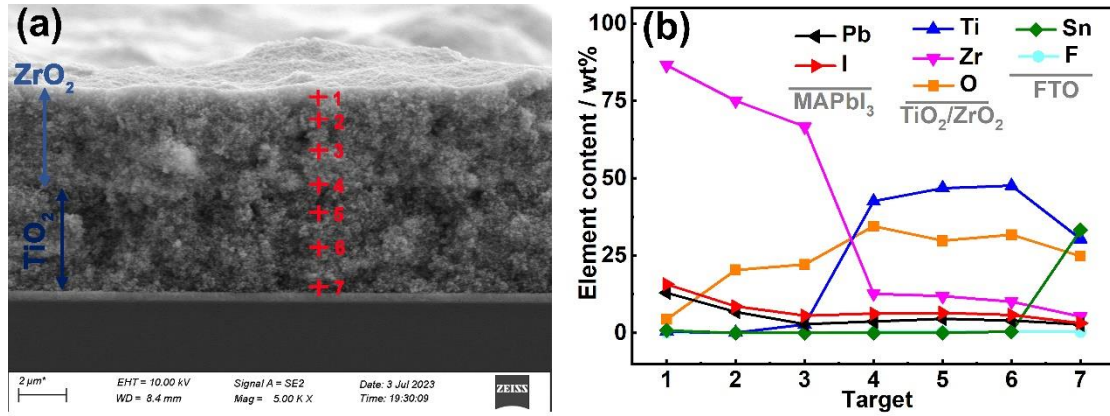


Fig. 1 Cross-sectional view of the TiO₂/ZrO₂ scaffold film filled with MAPbI₃ material, with seven selected targets marked by red crosses for element distribution analysis (a). Comparative weight percentage distribution of representative elements from MAPbI₃, TiO₂/ZrO₂, and FTO, based on targets 1 to 7 (b).

3.2 Optimization of perovskite precursor infiltration is the primary consideration to improve the filling amount

To understand the physical dynamics of the filling process, the infiltration process was first analyzed. The geometric structure of the TiO₂/ZrO₂ scaffold film was constructed for both 3D and 2D TiO₂/ZrO₂ models, as shown in Fig. 2(a) and 2(b). In the model, the lower layer consists of TiO₂, while the upper layer consists of ZrO₂. Since the thickness of the scaffold film (~6 μm) is much smaller than the length of the upper surface (~10 mm), evaporation from the lateral surface of the precursor solution can be neglected. Ideally, the MAPbI₃ solution permeates downward from the surface to the bottom, as illustrated in Fig. 2(c).

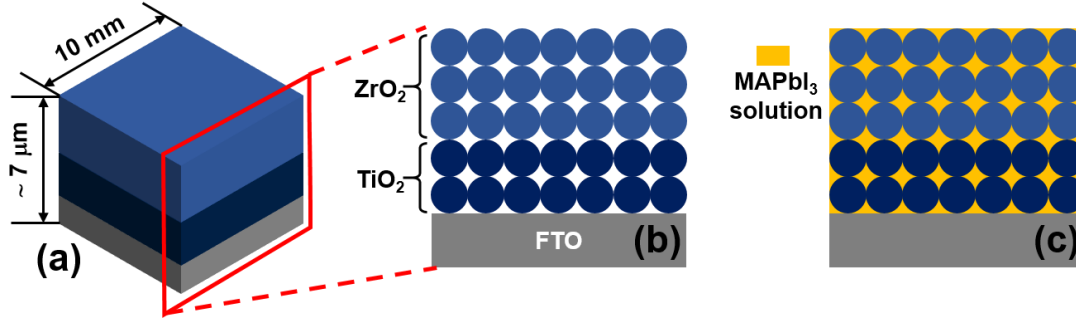


Fig. 2 Geometric structure of the $\text{TiO}_2/\text{ZrO}_2$ scaffold film: (a) 3D model, (b) 2D

model, and (c) complete infiltration of the MAPbI_3 precursor solution.

After depositing the MAPbI_3 precursor solution onto the $\text{TiO}_2/\text{ZrO}_2$ scaffold film, the infiltration length of the solution depends on both capillary attraction and evaporation. The evaporation rate of the MAPbI_3 precursor solution, denoted as V_1 , represents the rate at which the DMF solvent evaporates from the solution. Meanwhile, the infiltration rate, denoted as V_2 , represents the rate at which the perovskite precursor solution penetrates the scaffold film due to capillary attraction. These two opposing factors determine the filling amount and can be used to estimate the infiltration state. As shown in Fig. 3: When $V_1 > V_2$, strong evaporation prevents the perovskite precursor solution from penetrating deep into the $\text{TiO}_2/\text{ZrO}_2$ scaffold film, causing the perovskite material to accumulate in the upper region (Fig. 3(a)). When $V_1 = V_2$, the perovskite precursor solution crystallizes as it infiltrates, making it difficult for the perovskite material to reach the bottom of the scaffold film (Fig. 3(b)). When $V_1 < V_2$, the perovskite precursor solution has sufficient time to reach the bottom region of the $\text{TiO}_2/\text{ZrO}_2$ scaffold film, leading to deeper infiltration (Fig. 3(c)). If the entire mesoporous $\text{TiO}_2/\text{ZrO}_2$ scaffold film is fully immersed in the MAPbI_3 precursor solution, complete filling may be achieved depending on subsequent crystallization

conditions. Since V_1 is influenced by factors such as the porosity of the mesoporous framework, the wettability of materials, and solvent viscosity, optimizing the infiltration process requires strategies such as increasing pore size, enhancing wettability, and adjusting solvent properties. Additionally, reducing the evaporation rate can further improve infiltration, which can be achieved by conducting experiments in a cold and confined environment. In the following study, two specific strategies are chosen: increasing the pore size and maintaining the ambient temperature at 2–3°C.

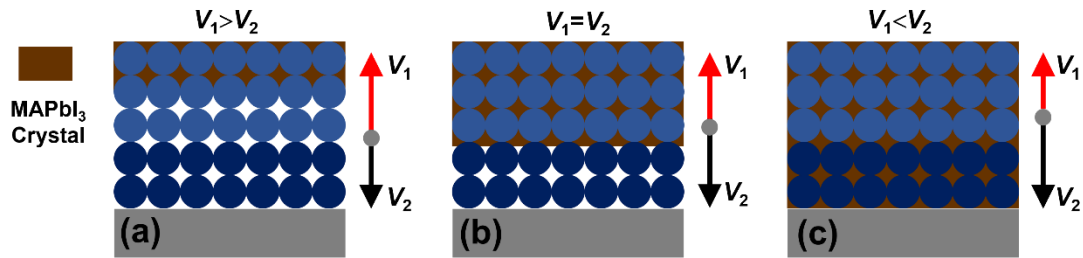


Fig. 3 Infiltration process influenced by the combined effect of both capillarity

attraction and evaporation: (a) $V_1 > V_2$, (b) $V_1 = V_2$ and (c) $V_1 < V_2$, where the

evaporation rate of DMF solvent is coded as V_1 , and the infiltration rate of the

MAPbI₃ precursor solution resulting from capillarity attraction is coded as V_2

3.3 Optimization of perovskite precursor crystallization is the secondary consideration to improve the filling amount

To further understand the physical dynamics of the filling process, the crystallization process was analyzed. The evaporation of the DMF solvent leads to solute accumulation in the upper region, creating a concentration gradient between the upper and bottom areas. As a result, the MAPbI₃ precursor diffuses from the upper region toward the bottom. Additionally, since DMF evaporation is an endothermic process, the temperature in the upper area decreases, forming a temperature gradient

1 between the upper and bottom regions. Given that the solubility of MAPbI₃ in DMF
2
3 decreases with decreasing temperature³⁹, the upper area of the precursor solution
4
5 becomes a preferential site for nucleation. Another preferential nucleation site is the
6
7 bottom region, as the energy barrier for heterogeneous nucleation is lower than that for
8
9 homogeneous nucleation⁴⁰.
10
11
12

13
14 If the preferential nucleation sites are confined to the upper region, nucleation and
15
16 growth of the MAPbI₃ precursor will occur sequentially on the surface of the TiO₂/ZrO₂
17
18 scaffold film as the DMF solvent evaporates, leading to a top-down crystallization
19
20 process, as shown in Fig. 4(a). If the crystallization is isotropic, the MAPbI₃ material
21
22 may cover the entire surface of the TiO₂/ZrO₂ scaffold film. Conversely, if the
23
24 preferential nucleation sites are located at the bottom, nucleation and growth of the
25
26 MAPbI₃ precursor will be concentrated in the lower region of the scaffold film. The
27
28 continuous evaporation of the DMF solvent will provide a driving force for bottom-up
29
30 crystallization, as shown in Fig. 4(b). In this case, perovskite will precipitate at the
31
32 bottom of the TiO₂/ZrO₂ scaffold film, and in combination with the bottom-up
33
34 crystallization process, this can result in complete filling. In the absence of
35
36 crystallization control, nucleation sites will be randomly distributed, leading to an
37
38 uncontrolled crystallization process where MAPbI₃ crystals form irregularly throughout
39
40 the TiO₂/ZrO₂ scaffold film, as illustrated in Fig. 4(c). In the following study, the
41
42 bottom-up crystallization process, assisted by a low-pressure gas pumping method, is
43
44 selected.
45
46
47
48
49
50
51
52
53
54
55
56
57
58
59
60
61
62
63
64
65

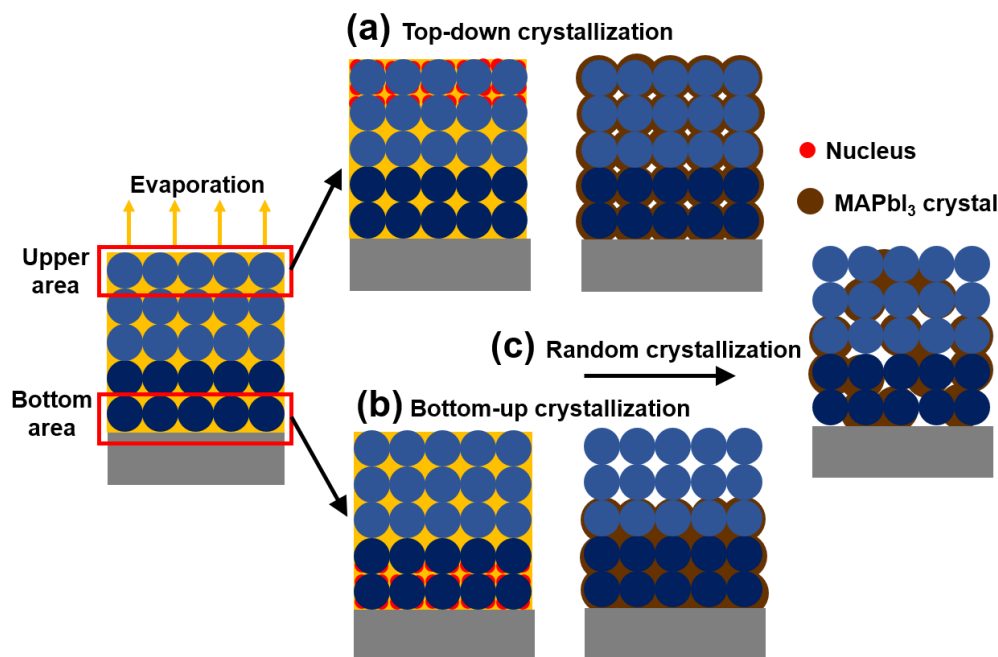


Fig. 4 Preferential nucleation sites and the corresponding filling states of MAPbI₃ based on different crystallization processes: (a) top-down crystallization dependent on the preferential nucleation site in the upper area, (b) bottom-up crystallization dependent on the preferential nucleation site in the bottom area, and (c) random crystallization dependent on uncontrollable nucleation sites.

3.4 The performance of PSCs with enhanced filling and those without enhancement was compared

Monodisperse PS microspheres are a type of material characterized by a highly uniform particle size distribution. They volatilize at temperatures above 200°C. When incorporated into a solid film and subsequently removed through annealing, they allow for direct regulation of the film's pore structure. To optimize the pore structure for enhancing the infiltration of the perovskite precursor solution, PS microspheres with a diameter of 300 nm were selected. The optimal amount of PS microspheres was determined through modeling calculations to maintain films with suitable porosity. The

1 detailed modeling and calculation process is provided in the supporting information.

2
3 The cross-sectional view of $\text{TiO}_2/\text{ZrO}_2$ scaffold with 25% porosity is shown in Figure
4
5
6 S7.
7

8
9 After the perovskite precursor solution has infiltrated the $\text{TiO}_2/\text{ZrO}_2$ scaffold film
10
11 with submicron pores, the sample is transferred to a low-pressure chamber to ensure
12
13 bottom-up crystallization. The element distribution of the final film is monitored using
14
15 EDS. Eight targets are selected, ranging from the upper area to the bottom area of the
16
17 film. As shown, the content of Pb and I elements remains nearly constant at 18 wt%
18
19 and 25 wt%, respectively, from target 1 to target 8. The filling of MAPbI_3 is clearly
20
21 enhanced from the upper surface to the bottom area of the scaffold layer. This result
22
23 highlights the importance of dividing the filling process of perovskite materials into
24
25 two critical stages: the infiltration of the perovskite precursor and the crystallization of
26
27 the solid perovskite. Complete filling in the first stage, followed by bottom-up
28
29 crystallization in the second stage, effectively promotes the full filling of perovskite
30
31 materials.
32
33
34
35
36
37
38
39
40
41
42
43
44
45
46
47
48
49
50
51
52
53
54
55
56
57
58
59
60
61
62
63
64
65

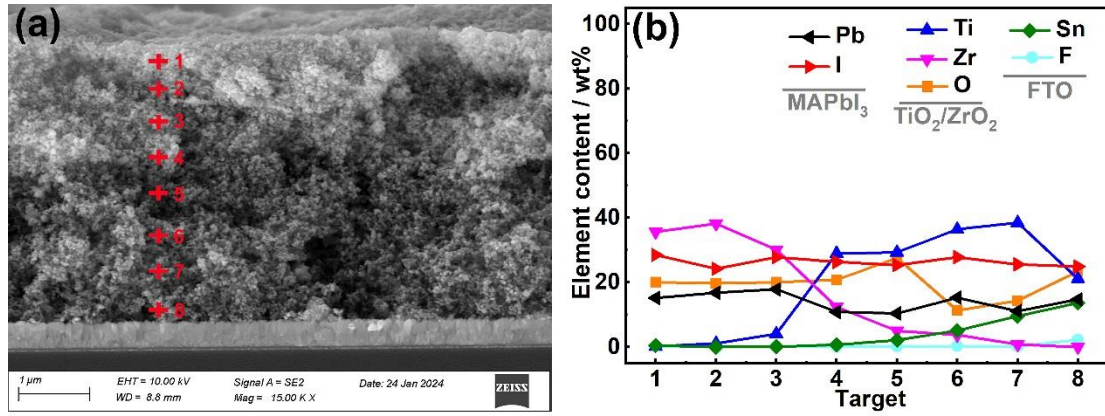


Fig. 5 Cross-sectional view of the TiO₂/ZrO₂ scaffold film with enhanced filling of MAPbI₃ material, showing the eight selected targets marked with red crosses for element distribution tracing (a). Comparative weight percent distribution of representative elements from MAPbI₃, TiO₂/ZrO₂, and FTO based on the targets from 1 to 8 (b).

When both the unenhanced-filling (Un-En) and enhanced-filling (En) scaffold films were assembled into PSCs, the typical photovoltaic performance is shown in Fig. 6. Both PSCs exhibit an open-circuit voltage (V_{oc}) of nearly 1.0 V, indicating that the P-N junction structure is intact and the voltage difference between the photoanode and counter electrode is consistent. However, the En PSC shows a short-circuit current density (J_{sc}) of 19.42 mA·cm⁻² and a fill factor (FF) of 57.51%, whereas the Un-En PSC shows a J_{sc} of 15.84 mA·cm⁻² and an FF of 16.47%. This improvement can be attributed to the enhanced perovskite filling in the scaffold layer, which both increases the light-harvesting capability of the cell and improves the perovskite/TiO₂ interface, facilitating carrier separation and transport while reducing the parallel resistance of the cell. Finally, the En PSC shows a conversion efficiency (η) of 10.60%, which represents a 375% improvement compared to the Un-En PSC. Furthermore, the batch stability of

the cell's photovoltaic performance was tested, as shown in Fig. 7. It can be observed that the mean values are $V_{oc} = 0.98$ V, $J_{sc} = 16.02$ mA·cm⁻², FF = 54.28%, and $\eta = 8.73\%$, demonstrating that enhancing the perovskite filling improves the stability of the cell structure, thereby achieving more stable performance.

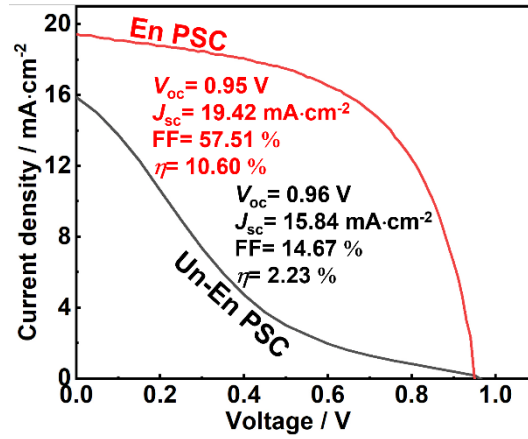


Fig. 6 Typical I - V results of the PSCs with the Un-En film (black line) and En film (red line)

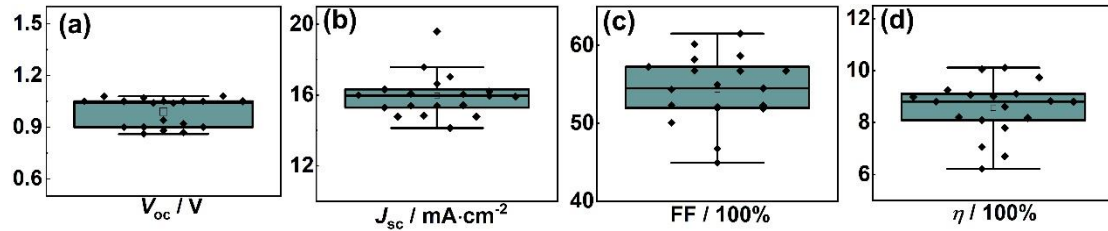


Fig. 7 Statistical results of the photovoltaic performance of the En PSCs: (a) V_{oc} , (b) J_{sc} , (c) FF and (d) η

4. Conclusion

In this study, the filling results show that MAPbI₃ tends to aggregate in the upper area of the TiO₂/ZrO₂ scaffold film. To enhance the filling of the perovskite material, a physical filling dynamics model has been systematically proposed. This model divides the filling process into two stages: the initial infiltration of the perovskite precursor solution and the subsequent bottom-up crystallization of the perovskite precursor. During the experiment, PS microspheres are introduced to enhance porosity, and the

temperature is kept low to restrain the evaporation of the solution. Additionally, bottom-up crystallization control is used to further improve perovskite incorporation into the scaffold layer. The EDS results show that the perovskite material is significantly filled within the inner part of the scaffold layer, and the photovoltaic performance confirms that increasing perovskite filling significantly enhances the conversion efficiency of the cells.

Acknowledgements

National Natural Science Foundation of China (Grant No. 62204202), Natural Science Basic Research Program of Shaanxi Province (Grant No. 2024JC-YBMS-438), Youth Innovation Team of Colleges and Universities in Shaanxi Province, The Key Research and Development Program of Shaanxi Program (Grant No. 2023KXJ-172), 2024 Scientific Research Project of Shaanxi Institute of technology (Grant No. Gfy24-04)

Availability of Supporting Data

Several supporting information has been added as a single text.

Conflict of Interest

All the authors declare of no conflict of interest.

Reference

1. Green, M. A.; Dunlop, E. D.; Yoshita, M.; Kopidakis, N.; Bothe, K.; Siefer, G.; Hao, X., Solar cell efficiency tables (version 62). *Prog. Photovolt.: Res. Appl.* **2023**, *31*, 651-663.
2. Chen, B.; Yu, Z.; Onno, A.; Yu, Z.; Chen, S.; Wang, J.; Holman, Z. C.; Huang, J., Bifacial all-perovskite tandem solar cells. *Sci. Adv.* **2022**, *8*, eadd0377.

3. Ku, Z.; Rong, Y.; Xu, M.; Liu, T.; Han, H., Full Printable processed mesoscopic $\text{CH}_3\text{NH}_3\text{PbI}_3/\text{TiO}_2$ heterojunction solar cells with carbon counter electrode. *Sci. Rep.* **2013**, *3*, 3132.
4. Mei, A.; Li, X.; Liu, L.; Ku, Z.; Liu, T.; Rong, Y.; Xu, M.; Hu, M.; Chen, J.; Yang, Y.; Grätzel, M.; Han, H., A hole-conductor-free, fully printable mesoscopic perovskite solar cell with high stability. *Science* **2014**, *345*, 295-298.
5. Liu, L.; Mei, A.; Liu, T.; Jiang, P.; Sheng, Y.; Zhang, L.; Han, H., Fully printable mesoscopic perovskite solar cells with organic silane self-assembled monolayer. *J. Am. Chem. Soc.* **2015**, *137*, 1790-1793.
6. Hu, Y.; Si, S.; Mei, A.; Rong, Y.; Liu, H.; Li, X.; Han, H., Stable large-area ($10 \times 10 \text{ cm}^2$) printable mesoscopic perovskite module exceeding 10% efficiency. *Solar RRL* **2017**, *1*, 1600019.
7. Fu, Z.; Xu, M.; Sheng, Y.; Yan, Z.; Meng, J.; Tong, C.; Li, D.; Wan, Z.; Ming, Y.; Mei, A.; Hu, Y.; Rong, Y.; Han, H., Encapsulation of printable mesoscopic perovskite solar cells enables high temperature and long-term outdoor stability. *Adv. Funct. Mater.* **2019**, *29*, 1809129.
8. Mei, A.; Sheng, Y.; Ming, Y.; Hu, Y.; Rong, Y.; Zhang, W.; Luo, S.; Na, G.; Tian, C.; Hou, X.; Xiong, Y.; Zhang, Z.; Liu, S.; Uchida, S.; Kim, T.-W.; Yuan, Y.; Zhang, L.; Zhou, Y.; Han, H., Stabilizing perovskite solar cells to IEC61215:2016 standards with over 9,000-h operational tracking. *Joule* **2020**, *4*, 2646-2660.
9. Rong, Y.; Hu, Y.; Mei, A.; Tan, H.; Saidaminov, M. I.; Seok, S. I.; McGehee, M. D.; Sargent, E. H.; Han, H., Challenges for commercializing perovskite solar cells.

Science **2018**, *361*, 5978.

10. Ito, S.; Tsuji, R. Mesoscopic anodes and cathodes for printable perovskite solar cells. 2023, Chapter 4.
11. Yao, Z.; Ning, Z. A breakthrough of printable mesoscopic perovskite solar cells. *Sci. Chi. Mater.* **2025**, *68*, 307-308.
12. Cao, K.; Zuo, Z.; Cui, J.; Shen, Y.; Moehl, T.; Zakeeruddin, S. M.; Grätzel, M.; Wang, M., Efficient screen printed perovskite solar cells based on mesoscopic TiO₂/Al₂O₃/NiO/carbon architecture. *Nano Energ.* **2015**, *17*, 171-179.
13. Duan, M.; Rong, Y.; Mei, A.; Hu, Y.; Sheng, Y.; Guan, Y.; Han, H., Efficient hole-conductor-free, fully printable mesoscopic perovskite solar cells with carbon electrode based on ultrathin graphite. *Carbon* **2017**, *120*, 71-76.
14. Jiang, P.; Jones, T. W.; Duffy, N. W.; Anderson, K. F.; Bennett, R.; Grigore, M.; Marvig, P.; Xiong, Y.; Liu, T.; Sheng, Y.; Hong, L.; Hou, X.; Duan, M.; Hu, Y.; Rong, Y.; Wilson, G. J.; Han, H., Fully printable perovskite solar cells with highly-conductive, low-temperature, perovskite-compatible carbon electrode. *Carbon* **2018**, *129*, 830-836.
15. Xu, C.; Zhang, Z.; Hu, Y.; Sheng, Y.; Jiang, P.; Han, H.; Zhang, J., Printed hole-conductor-free mesoscopic perovskite solar cells with excellent long-term stability using PEAi as an additive. *J. Energ. Chem.* **2018**, *27*, 764-768.
16. Jeon, N. J.; Noh, J. H.; Kim, Y. C.; Yang, W. S.; Ryu, S.; Seok, S. I., Solvent engineering for high-performance inorganic–organic hybrid perovskite solar cells. *Nat. Mater.* **2014**, *13*, 897-903.

17. Wu, Y.; Islam, A.; Yang, X.; Qin, C.; Liu, J.; Zhang, K.; Peng, W.; Han, L., Retarding the crystallization of PbI₂ for highly reproducible planar-structured perovskite solar cells via sequential deposition. *Energ. Environ. Sci.* **2014**, *7*, 2934-2938.
18. Ahn, N.; Son, D.-Y.; Jang, I.-H.; Kang, S. M.; Choi, M.; Park, N.-G., Highly reproducible perovskite solar cells with average efficiency of 18.3% and best efficiency of 19.7% fabricated via lewis base adduct of lead(II) iodide. *J. Am. Chem. Soc.* **2015**, *137*, 8696-8699.
19. Hou, X.; Xu, M.; Tong, C.; Ji, W.; Fu, Z.; Wan, Z.; Hao, F.; Ming, Y.; Liu, S.; Hu, Y.; Han, H.; Rong, Y.; Yao, Y., High performance printable perovskite solar cells based on Cs_{0.1}FA_{0.9}PbI₃ in mesoporous scaffolds. *J. Power Sources* **2019**, *415*, 105-111.
20. Chen, J.; Rong, Y.; Mei, A.; Xiong, Y.; Liu, T.; Sheng, Y.; Jiang, P.; Hong, L.; Guan, Y.; Zhu, X.; Hou, X.; Duan, M.; Zhao, J.; Li, X.; Han, H., Hole-conductor-free dully printable mesoscopic solar cell with mixed-anion perovskite CH₃NH₃PbI_(3-x)(BF₄)_x. *Adv. Energ. Mater.* **2016**, *6*, 1502009.
21. Wang, Q.; Zhang, W.; Zhang, Z.; Liu, S.; Wu, J.; Guan, Y.; Mei, A.; Rong, Y.; Hu, Y.; Han, H., Crystallization control of ternary-cation perovskite absorber in triple-mesoscopic layer for efficient solar cells. *Adv. Energ. Mater.* **2020**, *10*, 1903092.
22. Saliba, M.; Matsui, T.; Seo, J.-Y.; Domanski, K.; Correa-Baena, J.-P.; Nazeeruddin, M. K.; Zakeeruddin, S. M.; Tress, W.; Abate, A.; Hagfeldt, A.; Grätzel, M., Cesium-containing triple cation perovskite solar cells: improved stability, reproducibility

- and high efficiency. *Energ. Environ. Sci.* **2016**, 9, 1989-1997.
23. Saliba, M.; Matsui, T.; Domanski, K.; Seo, J.-Y.; Ummadisingu, A.; Zakeeruddin, S. M.; Correa-Baena, J.-P.; Tress, W. R.; Abate, A.; Hagfeldt, A.; Grätzel, M., Incorporation of rubidium cations into perovskite solar cells improves photovoltaic performance. *Science* **2016**, 354, 206-209.
24. Xiang, J.; Han, C.; Cheng, Y.; Gao, Q.; Hu, W.; Zhou, Y.; Mei, A.; Zhou, Y.; Han, H. Recent progress and advances of perovskite crystallization in carbon-based printable mesoscopic solar cells. *Adv. Mater.* **2025**, 2415405.
25. Li, F.; Lin, F. R.; Jen, A. K. Y. Current state and future perspectives of printable organic and perovskite solar cells. *Adv. Mater.* **2024**, 36, 2307161.
26. Yang, H.; Zhao, J.; Zhou, T.; Zhang, H.; Zhang, W.; Zhang, J.; Hu, G.; Zhang, Y.; Liu, Q. Mesoporous TiO₂ electron transport materials derived from 2D Ti-MOFs for enhanced power conversion efficiency in Pprinted mesoscopic perovskite solar cells. *ACS Appl. Nano Mater.* **2023**, 6, 16353-16361.
27. Worsley, C. A.; Dunlop, T. O.; Potts, S.-J.; Garcia-Rodriguez, R.; Bolton, R. S.; Davies, M. L.; Jewell, E.; Watson, T. M. Quantifying infiltration for quality control in printed mesoscopic perovskite solar cells: a microscopic perspective. *ACS Appl. Energ. Mater.* **2024**, 7, 1938-1948.
28. Xiang, J.; Han, C.; Qi, J.; Cheng, Y.; Chen, K.; Ma, Y.; Xie, J.; Hu, Y.; Mei, A.; Zhou, Y. A Polymer defect passivator for efficient hole-conductor-free printable mesoscopic perovskite solar cells. *Adv. Funct. Mater.* **2023**, 33, 2300473.
29. Wang, H.; Yang, F.; Li, X.; Zhang, P. Fully printed high-performance quasi-

two-dimensional perovskite solar cells via multifunctional interfacial engineering.

Adv. Funct. Mater. **2024**, *34*, 2312250.

30. Chen, J.; Xiong, Y.; Rong, Y.; Mei, A.; Sheng, Y.; Jiang, P.; Hu, Y.; Li, X.; Han, H., Solvent effect on the hole-conductor-free fully printable perovskite solar cells. *Nano Energ.* **2016**, *27*, 130-137.
31. Rong, Y.; Venkatesan, S.; Guo, R.; Wang, Y.; Bao, J.; Li, W.; Fan, Z.; Yao, Y., Critical kinetic control of non-stoichiometric intermediate phase transformation for efficient perovskite solar cells. *Nanoscale* **2016**, *8*, 12892-12899.
32. Jiang, Z.; Wang, B.; Zhang, W.; Yang, Z.; Li, M.; Ren, F.; Imran, T.; Sun, Z.; Zhang, S.; Zhang, Y.; Zhao, Z.; Liu, Z.; Chen, W., Solvent engineering towards scalable fabrication of high-quality perovskite films for efficient solar modules. *J. Energ. Chem.* **2023**, *80*, 689-710.
33. Bogachuk, D.; Girard, J.; Tilala, S.; Martineau, D.; Narbey, S.; Verma, A.; Hinsch, A.; Kohlstädt, M.; Wagner, L. Nanoarchitectonics in fully printed perovskite solar cells with carbon-based electrodes. *Nanoscale* **2023**, *15*, 3130-3134.
34. Gao L.; Yang G. J. Organic-inorganic halide perovskites: from crystallization of polycrystalline films to solar cell applications *Solar RRL* **2019**, *12*, 1900200.
35. Ding B.; Li Y.; Huang S. Y.; Chu Q. Q.; Li C. X.; Li C. J.; Yang G. J.; Material nucleation/growth competition tuning towards highly reproducible planar perovskite solar cells with efficiency exceeding 20% *J. Mater. Chem. A* **2017**, *5*, 6840-6848.
36. Ding B.; Gao L. L.; Liang L. S.; Chu Q. Q.; Song X. X.; Li Y.; Yang G. J.; Fan B.;

1 Wang M. K.; Li C. X.; Li C. J. Facile and scalable fabrication of highly efficient
2
3 lead iodide perovskite thin-film solar cells in air using gas pump method, *ACS Appl.*
4
5
6 *Mater. Interf.* **2016**, 8, 20067-20073.
7

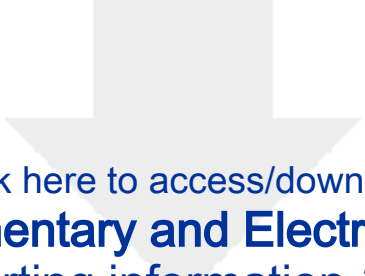
8
9 37. Zhao, Y.; Zhu, K., Solution chemistry engineering toward high-efficiency
10
11 perovskite solar cells. *J. Phys. Chem. Lett.* **2014**, 5, 4175-4186.
12
13

14 38. Han, H.; Bach, U.; Cheng, Y.-B.; Caruso, R. A.; MacRae, C., A design for
15
16 monolithic all-solid-state dye-sensitized solar cells with a platinized carbon
17
18 counterelectrode. *Appl. Phys. Lett.* **2009**, 94, 103102.
19
20
21

22 39. Heo, J. H.; Song, D. H.; Im, S. H., Planar CH₃NH₃PbBr₃ hybrid solar cells with
23
24 10.4% power conversion efficiency, fabricated by controlled crystallization in the
25
26 spin-coating process. *Adv. Mater.* **2014**, 26, 8179-8183.
27
28
29

30 40. Li, Y.; Li, X.; Chu, Q.; Dong, H.; Yao, J.; Zhou, Y.; Yang, G., Tuning nucleation
31
32 sites to enable monolayer perovskite films for highly efficient perovskite solar cells.
33
34
35
36
37 *Coatings* **2018**, 8, 408.
38
39
40
41
42
43
44
45
46
47
48
49
50
51
52
53
54
55
56
57
58
59
60
61
62
63
64
65

-
- $\text{CH}_3\text{NH}_3\text{PbI}_3$ aggregates at the upper area of $\text{TiO}_2/\text{ZrO}_2$ scaffold film.
 - Filling process should be divided into infiltration and precipitation.
 - Increasing pore size combined with bottom-up crystallization promote filling.
 - η of En PSC improves by 375% compared with Un-En PSC.



[Click here to access/download](#)
Supplementary and Electronic files
Supporting information-3.docx

